SAND2020-10376C

# Development of an Aerial Imaging System for Heliostat Canting Assessments

Julius Yellowhair[1, a)], Pavlos A. Apostolopoulos[2], Daniel E. Small[3, b)],
David Novick[3], and Micah Mann[3]

[1]*Gryphon Technologies, 2309 Renard Pl SE #120, Albuquerque, NM 87131 USA.*
[2]*Univeristy of New Mexico, Department of Electrical and Computer Engineering, Albuquerque, NM 87131 USA.*
[3]*Sandia National Laboratories, P.O. Box 5800, Albuquerque, NM 87185 USA.*

[a)] Corresponding author: jey422@gmail.com
[b)] desmall@sandia.gov

**Abstract.** The heliostat collector field is the front-end of large solar power tower plants. Any negative performance impacts on the collector field will propagate down the stream of subsystems, which can negatively impact energy production and financial revenues. An underperforming collector field will provide insufficient solar flux to the receiver resulting in the receiver running at below capacity and not producing the thermal energy required for thermal storage and to run the power block at optimum efficiency. It is prudent to have an optimally operating collector field especially for future Gen3+ plants. The performance of a deployed collector field can be impacted by mirror quality (surface and shape), mirror canting errors, tracking errors, and soiling. Any of these error sources can exist during installation and further degrade over time and, if left unattended, can drastically reduce the overall performance of the plant. Concentrating solar power (CSP) plant operators require information about the collector field performance to quickly respond with corrections, if needed, and maintain optimum plant performance. This type of fast response is especially critical for future Gen3+ plants, which require high collector field performance consistently. However, power tower operators have struggled with finding or developing the right tools to assess and subsequently fix canting errors on in-field heliostats efficiently and accurately. Sandia National Laboratories National Solar Thermal Test Facility (NSTTF) is developing an aerial imaging system to evaluate facet canting quality on in-situ and offline heliostats. The imaging system is mounted on an unmanned aerial system (UAS) to collect images of targets structures in reflection. Image processing on the collected images is then performed to get estimates of the heliostat canting errors. The initial work is to develop the system definition that achieves the required measurement sensitivities, which is on the order of 0.25-0.5 mrad for canting errors. The goal of the system is to measure heliostat canting errors to < 0.5 mrad accuracy and provide data on multiple heliostats within a day. In this paper, the development of the system, a sensitivity analysis, and initial measurement results on two NSTTF heliostats are provided.

## INTRODUCTION

Increasing demand for energy worldwide and concerns over climate change have brought needs to further develop renewable energy technologies such as wind, geothermal, and solar power. Solar energy systems have shown high potential for large-scale energy production. In particular, central receiver power towers are regarded as a proven concentrating solar power (CSP) technology with the potential for high energy production and significant cost reductions [1].

In power tower systems, a heliostat collector field is used to reflect solar energy on to a central receiver located at the top of a tower. Each heliostat in the field typically consists of structurally mounted mirror surfaces which can be rotated to continuously reflect sunlight on to the central receiver. Most commercial central receiver systems use the energy collected from the heliostat field to heat a fluid circulating through the receiver. The fluid is then used to create steam to generate electricity through steam-turbine technologies commonly employed in other power plants. Figure 1 shows the Sandia National Laboratories National Solar Thermal Test Facility (NSTTF) solar tower and heliostat field

Sandia National Laboratories is a multimission laboratory managed and operated by National Technology & Engineering Solutions of Sandia, LLC, a wholly owned subsidiary of Honeywell International Inc., for the U.S. Department of Energy's National Nuclear Security Administration under contract DE-NA0003525.

located in Albuquerque, New Mexico, USA. The NSTTF is not a commercial facility but a research facility ideal for developing measurement tools for commercial applications.

**FIGURE 1.** Sandia NSTTF solar tower and the heliostat field.

Most heliostats are composed of an array of smaller mirror facets, on the order of 1-2 $m^2$, on a single rotating frame. In a commercial plant, the performance of the collector field can be impacted by mirror quality (surface and shape), mirror canting errors, tracking errors, and soiling. Any of these error sources can exist during installation and further degrade over time. If left unattended, the optical errors can drastically reduce the overall performance of the plant. CSP plant operators require information about the collector field performance to quickly respond with corrections, if needed, and maintain optimum plant performance. However, CSP operators in most cases do not have access to accurate and efficient tools to make field measurements to get accurate information on collector field performance. In this work, a measurement tool using aerial imaging is described to assess heliostat facet canting errors.

Large canting errors in heliostats can cause beam spillage at the receiver, which is energy lost and unrecovered. They can also create irregular beam shapes at the receiver or beam characterization target, which makes centroiding the beam difficult for tracking error estimates and could also create hot spots on the receiver. The need for assessing and correcting facet canting errors has brought about a number of measurement and correction techniques. Techniques that have been used include photogrammetry, visual beam quality observations (i.e., the on-sun alignment technique), laser beam projections, using inclinometers, and other mechanical and optical methods. However, these techniques typically have properties which make them time-consuming or inaccurate [2].

To overcome the limitations of the various measurement and alignment techniques, Sandia has previously developed a unique alignment tool called the Heliostat Focusing and Canting Enhancement Technique (HFACET) [3-4]. HFACET is an optical method which allows for fast and accurate detection and correction of heliostat canting errors. HFACET utilizes a camera fixed on top of the tower, an in-field target, and a computer running MATLAB for image collection or video display and image processing. During the measurement and alignment process, a heliostat is rotated to reflect the image of the in-field target to the camera located at the tower top. The camera captures a video of the reflected target image. This video is received by the computer and compared to the target's theoretical reflected appearance as computed by the custom MATLAB script. The difference between the theoretical and actual appearance of the reflected target is then used by a technician to identify and correct the canting errors present in the heliostat. HFACET can assess both facet canting and focusing. HFACET was successfully implemented at NSTTF and used to recant all 200+ heliostats after the mirror facets were replaced. The new work extends the capabilities of HFACET.

## APPROACH

Previously Sandia successfully developed and implemented a target reflection approach, called HFACET, to assess heliostat facet canting quality at the NSTTF [3-4]. The system also provided feedback for making corrections to the measured facet canting errors. It was estimated the system corrected the facet errors to better than 0.3 mrad root mean square (RMS) [4]. The previous system consisted of a fixed machine-vision camera with a zoom lens on top of the tower as shown in Figure 2a. The camera on a tripod was pointed at a heliostat to be assessed. The heliostat was rotated so that a target structure can be seen in reflection. The target structure can be a frame structure on wheels that can be transported around the field or a neighboring heliostat that is already in the field. By knowing the geometric dimensions of the target structure and its location relative to the heliostat under assessment, its ideal image in reflection can be calculated. This ideal image can be overlaid on the actual camera image or video of the target in reflection. Differences between the actual and ideal (theoretically calculated) image of the target structure reveal the facet canting errors present in the heliostat. The system worked well for the NSTTF field, but a couple of limitations were identified if extended to large commercial fields. At the NSTTF, the longest heliostat slant range to the tower is about 220 m. In large commercial power tower plants, heliostat slant ranges can approach 1600 m (~1 mile) at the edge of the field. One limitation of HFACET was the fixed camera position on top of the tower. At longer slant ranges (>1000 m), bigger zoom lenses are needed. High optical quality zoom lens, for example telescopes, can become costly. Without large zoom lenses, the image resolution is reduced for long slant range heliostats. This can significantly reduce the accuracy of the system in estimating the canting errors. The other limitation is the camera needs to be high on the tower to see all the heliostats. Lowering the camera starts to cause obstructions between heliostats.

In the new development (UFACET or Universal Field Assessment, Correction, and Enhancement Tool), the camera becomes mobile therefore the issue with large slant ranges or the fixed camera position is eliminated (see Figure 2b). The camera mobility is made possible with an unmanned aerial system (UAS), otherwise known as a drone. The camera can be moved closer to any heliostat in the field. The target structure can be provided by a neighboring heliostat. With the mobile camera, additional advantages can also be realized: the heliostats can be measured while in-situ or offline. In the case of in-situ measurements, disruptions to the plant operation is minimized as only the camera position needs to be determined from the heliostat tracking positions to collect the needed images, although some constraints need to be applied to ensure measurement accuracy. One constraint is to keep the camera view angle (i.e., angle between the camera line-of-sight and the heliostat surface normal vector or pointing direction) below a threshold, for example < 30°. This ensures high pixel density over the whole heliostat under assessment. An additional advantage is since the camera can move to any heliostat in the field, the issue of long slant ranges in large commercial plants is eliminated. Therefore, the system is scalable to any size commercial field.

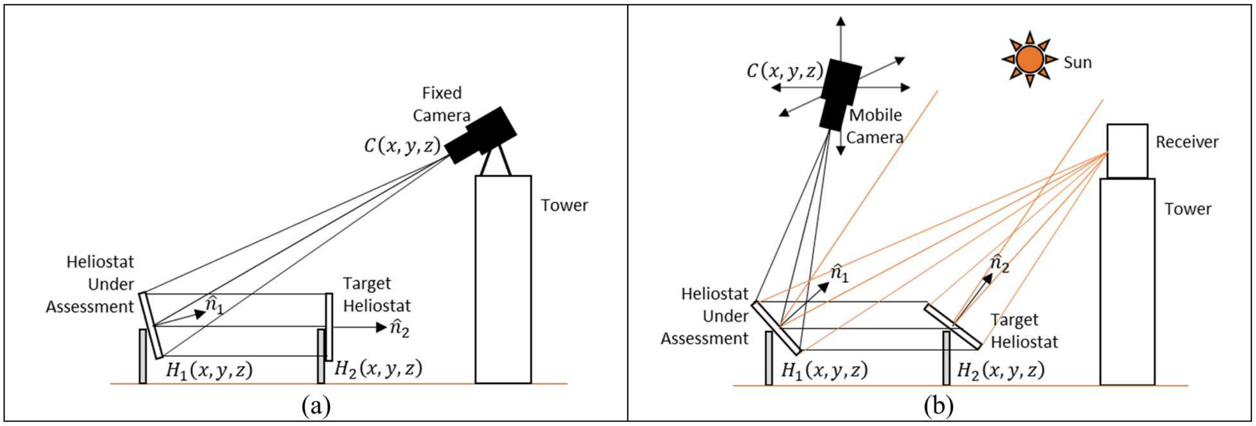

(a) (b)

**FIGURE 2.** (a) Camera on a fixed platform with the heliostats offline. (b) Camera on a mobile platform with in-situ heliostats.

The UFACET system is being developed using the Sandia NSTTF heliostat field. Figure 3 shows schematics of the NSTTF heliostat on the front and backsides (left and center) as well as an actual image of a heliostat (right). Also shown is the facet numbering scheme, which corresponds to the plots provided in the Results and Discussion section. Table 1 shows the parameters of the NSTTF heliostats. Canting quality is measured for each of the 25 facets, and the errors are reported in azimuth and elevation facet angles in their local coordinate system.

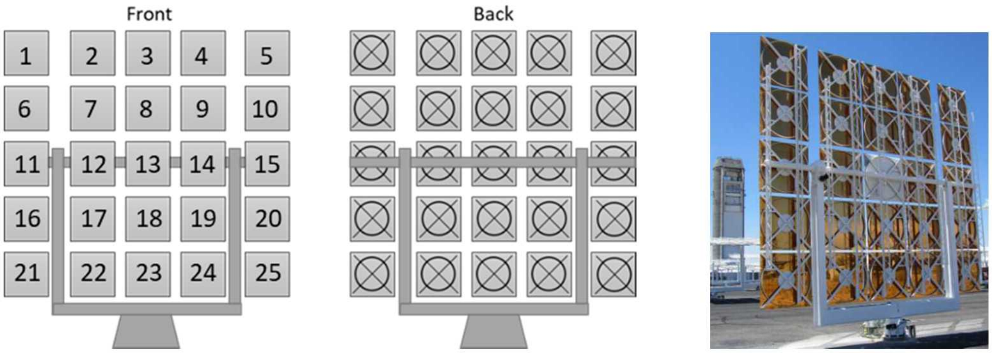

**FIGURE 3.** Schematics of Sandia NSTTF heliostat on the (left) front, (center) backside, and (right) actual image of the heliostat.

**TABLE 1.** NSTTF heliostat parameters.

| Parameter | Value |
|---|---|
| Facet size | 1.22 m × 1.22 m |
| Heliostat size | 6.81 m (H) × 6.35 (V) m |
| Number of facets | 25 (5 × 5) |
| Facet attachment | 3 bolts |

## Camera Positioning

The camera position calculation depends on the orientations of the heliostat pair while they are in-situ (Figure 4) or offline (Figure 5). In either case, the target structure (e.g., a neighboring heliostat) at the center is reflected at the center of the heliostat under assessment. The reflected ray at $H_1$ becomes the camera line-of-sight vector. For the in-situ case, the surface normal vector of the assessed heliostat can be derived from the reflection equation by knowing the sun position, $S$, heliostat position, $H_1$, and the aimpoint, $T$, all in three-dimensional coordinates [5]. The normalized vectors are first defined as:

$$\overrightarrow{H_1S} = (S - H_1)/|S - H_1|$$
$$\overrightarrow{H_1T} = (T - H_1)/|T - H_1|$$

Then the surface normal vector of the heliostat is calculated.

$$\hat{n}_1 = \frac{\overrightarrow{H_1S} + \overrightarrow{H_1T}}{\sqrt{2 + 2\left(\overrightarrow{H_1S} \cdot \overrightarrow{H_1T}\right)}}$$

After the assessed heliostat surface normal vector, $\hat{n}_1$, is determined, the "ray" connecting the centers of the target heliostat, $H_2$, and the assessed heliostat, $H_1$, can be reflected using the reflection equation again starting with normalized vectors.

$$\overrightarrow{H_1C} = (C - H_1)/|C - H_1|$$
$$\overrightarrow{H_1H_2} = (H_2 - H_1)/|H_2 - H_1|$$

$$\overrightarrow{H_1C} = -\overrightarrow{H_1H_2} + 2\left(\overrightarrow{H_1H_2} \cdot \hat{n}_1\right)\hat{n}_1$$

The vector, $\overrightarrow{H_1C}$, becomes the camera line-of-sight, where $C$ is the camera entrance pupil position coordinate. The camera can be placed at some distance, $D$, along this line-of-sight vector. The distance, $D$, depends on three factors: 1) heliostat size, 2) required image size of the target in reflection on the heliostat under assessment, and 3) the measurement sensitivity. The size of the NSTTF heliostats is provided in Table 1. To get the size of the reflected target image (in this case a neighboring heliostat) to cover about 60% of the assessed heliostat area, the distance, $D$, should be around $4 \cdot d$, where $d$ is the separation distance between the assessed and target heliostat. For the NSTTF heliostats, 60% area coverage allows for assessment of the whole heliostat in a single image. Figure 6 shows examples of a target heliostat seen in reflection through the heliostat under assessment.

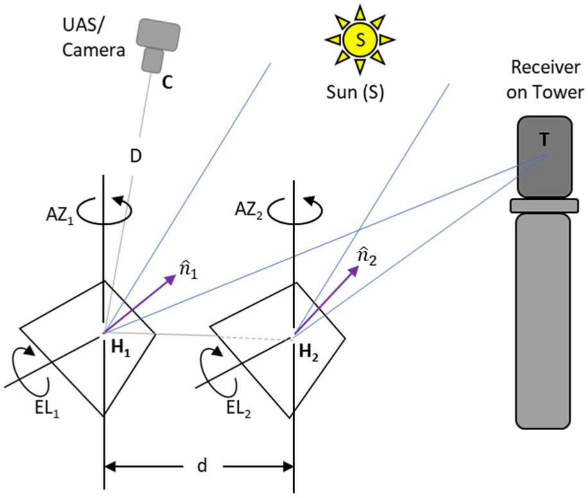

**FIGURE 4.** Measurement geometry for in-situ heliostats.

In the offline case (i.e., non-tracking heliostats), the heliostat angles are pre-calculated to place the camera at a convenient location or to allow constraints to be met to ensure high accuracy in the measurements.

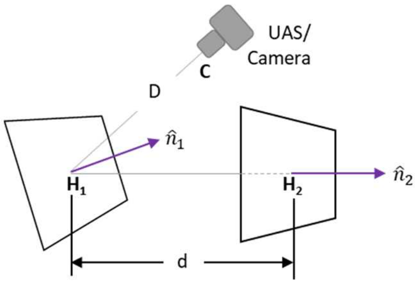

**FIGURE 5.** Measurement geometry example for offline heliostats.

The measurement sensitivity is improved by increasing the camera distance, $D$. However, the camera distance must be balanced with the available camera lens focal length and the slope errors in facet. If $D$ is increased, the lens focal length must be sufficient to maximize the extent of the assessed heliostat image in the camera field-of-view, otherwise the pixel density on the heliostat image is reduced which reduces the measurement sensitivity. It is beneficial to use a high pixel density camera sensor such as a 1/2.3-inch sensor along with a zoom lens with sufficient focal length zoom range. The other drawback of increasing $D$ is the impact of the facet slope errors. High slope errors will degrade the reflected image quality quickly, in which case the distance $D$ needs to be shortened to distinguish the reflected target features. Considerations should be made when working with mirror facets that have high slope errors as these will impact the canting error estimations.

## Canting Assessment Modes

The analysis code, written in Matlab, was developed to allow for multiple assessment modes. For example, the assessed heliostat can be assumed to have flat or curved facets. In the future, actual measured shapes of the facets can be incorporated for improved accuracy of the measurements. The effect of the facet shape selection is the surface slopes across the facet changes, which will impact the reflected location of the target feature that is used to calculate the canting errors. Although this impact is small since the heliostat facet focal lengths are very long (i.e., tens to thousands of meters) that they are almost flat, it is prudent to get as much accuracy as possible from the measurements because the stack up of errors and uncertainties can grow quickly.

The analysis code also provides the option to calculate facet canting errors based on an 1) on-axis or 2) off-axis canting strategy, or 3) a flat heliostat. In the on-axis canting strategy, the heliostat, its aimpoint (which could be the receiver location), and the sun are assumed to be in a line; that is, the aimpoint and the sun lie on the heliostat optical axis. The incoming sun rays are then reflected off the facets such that the reflected beams from all the facets intersect at the aimpoint location. This creates an axisymmetric parabolic heliostat shape with a focal length that is equal to the distance between the heliostat and the aimpoint. In the off-axis canting strategy, the sun position is determined for a specific day and time, e.g., day 80 (spring equinox) at solar noon for the location of the collector field. The sun is no longer in line with the heliostat and the aimpoint. The reflected beams from all the facets intersect at the aimpoint location. This creates an astigmatic heliostat shape. Depending on the heliostat position in the field, each heliostat will have a different level of astigmatism. In the flat heliostat case, all the facet surface normal vectors are parallel. Typically, flat heliostats are not used in solar power towers but can be used for solar furnaces where it is combined with a fixed parabolic dish to concentrate sunlight. Depending on the assessment modes chosen, the analysis code, from the heliostat images taken, will calculate facet angle deviations from the ideal alignment and report these as canting errors. The reported canting errors can then be printed out for technicians to apply to the heliostats through angle adjustments of the facets.

## Example Heliostat Images

Figure 6 shows images of heliostat 9W1 (read as row 9, first column from center to the west) with heliostat 8W1 in reflection while both heliostats are tracking to a standby aimpoint in the morning of 04/08/2020. Images were collected with a commercial UAS. In the left image the camera distance from the assessed heliostat (9W1) was about 4·d, where d is the separation distance between 9W1 and 8W1 heliostats. In the right image, the camera distance is increased to about 5·d. There are two things to note in the images. First, the UAS integrated camera zoom lens did not have large enough focal length lens to maximize the heliostat size in the field-of-view. As the camera is moved back to 5·d, the heliostat image becomes even smaller. The impact of this is reduced pixel density over the heliostat which reduces our accuracy to perform edge detections, target feature detections, and photogrammetry. In the future, a larger zoom lens that we have identified will be utilized. Second, for NSTTF heliostats, at a camera distance of 4·d (left image) the reflected image of 8W1 covers about 60% of the area on 9W1. This allows us to perform an analysis on the whole heliostat with one image. Note as the camera is moved back to 5·d (right image), the reflected image grows bigger and the measurement sensitivity gets better. However, the heliostat (9W1) image gets smaller and thus the measurement sensitivity gain is lost due to the effective low image resolution. A larger zoom lens is needed to fill the heliostat in the camera field-of-view.

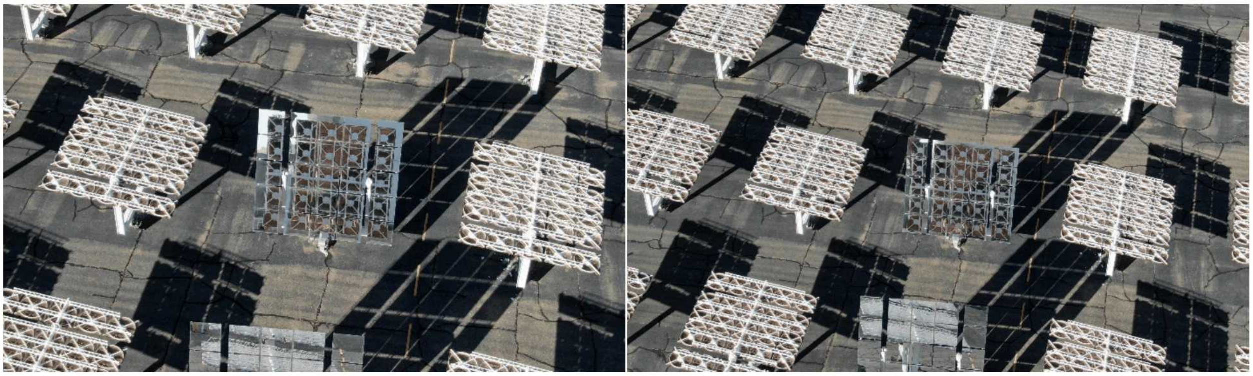

**FIGURE 6.** UAS images of heliostat 9W1, with 8W1 in reflection, at camera distances of (left) 4·d and (right) 5·d, where d is the distance between 9W1 and its target heliostat, 8W1.

After images are collected with UAS camera, the images are uploaded into the analysis code for processing. The process includes identifying the assessed heliostat edges and corners and reflected target features in the image. Figure 7 shows several examples of detecting different target features in the images, which in this case consists of the backside facet structure seen in reflection through one facet. The top row of images shows the identification of the reflected small circular plate with several points, and a general elliptical shape is fitted to the points. The center of the fitted elliptical shape is marked with a red star. The blue star marks where the center of the circular target plate should be if this particular facet was correctly aligned for the specified aimpoint and canting strategy. Therefore, the separation of the red and blue stars is a measure of the canting error for this facet. The separation can be decomposed into horizontal and vertical directions to get the canting errors in azimuth and elevation directions. The bottom row of images shows a similar process using the large outer hoop as the target feature.

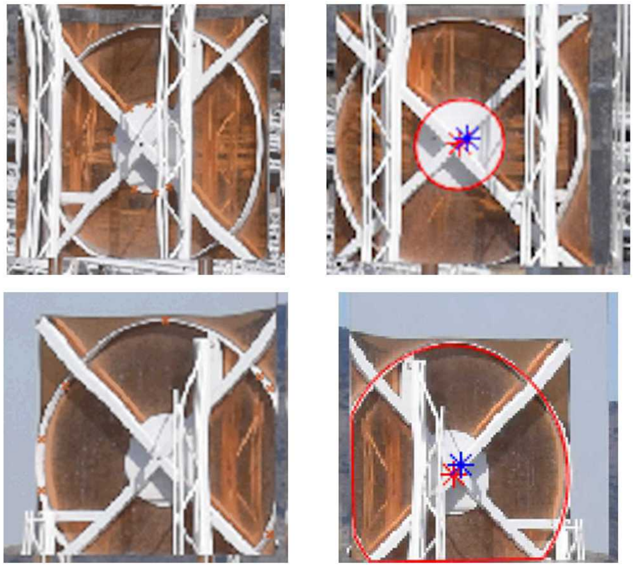

**FIGURE 7.** Examples of reflected target features in a facet.

We also use the facet backside crossmembers as the target feature. The results provided in the next section are from using the crossmembers as target features. The analysis code uses a reverse ray-tracing algorithm that uses an optimization scheme to map any number of points from a target feature of any structure and shape onto the heliostat under assessment assuming a viewpoint from the camera position. With the corners of the heliostats identified in the image, the theoretically mapped points are overlaid on the image by matching up the corner points from the image and theoretically determined map.

Figure 8 shows examples of target feature mapping onto the heliostat images. The mapped features in red locate where the actual feature images should be if the facet were properly aligned. In the left image the crossmember features are mapped and compared to the locations of the actual images of the crossmembers. Differences (between mapped features and actual feature images) give a measure of the facet canting errors. In the right image, the small circular plate and large circular hoop are mapped and can be compared to the locations of their corresponding images. With the circular hoop target features, not only can we get a measure of the facet canting errors from difference in positions of the mapped and actual features, we can also get a measure of the facets shape deviation from their design shapes by comparing the sizes of the mapped features to the sizes of the actual feature images. The work to date has not considered assessing or measuring the facet shapes to determine their focal lengths.

**FIGURE 8.** Example of target mapping on heliostat 5W3: (left) mapping of crossmember features and (right) mapping of circular hoops in red.

## RESULTS AND DISCUSSION

In this section, we provide some initial results on images collected on two heliostats: 5W9 and 9W1. Table 2 shows the coordinates and slant ranges of the two heliostats. The origin of the field coordinate system is at the center base of the tower with the x-axis pointing east and y-axis point north.

**TABLE 2.** Heliostat positions and slant range.

| Heliostat ID | Base Coordinates (m) | Slant Range (m) |
|---|---|---|
| 5W9 | (-82.0, 57.9, 2.6) | 109.1 |
| 9W1 | (-4.9, 107.3, 4.3) | 112.8 |

Assuming curved facets (i.e., curved to slant range) and an on-axis canting strategy, Figure 9 plots the calculated canting errors from the UFACET system for all 25 facets on heliostat 5W9 (blue bars). See Figure 3 for the facet numbering scheme. For comparison, the same heliostat was measured with a commercial LIDAR system [6]. The results from the LIDAR system are plotted as orange bars. The left plot shows the canting errors in the local facet azimuth direction, and the right plot shows the errors in local facet elevation angle. The RMS difference in the canting error estimates between the UFACET method and the LIDAR system on all 25 facets was around 0.8 mrad for both azimuth and elevation directions.

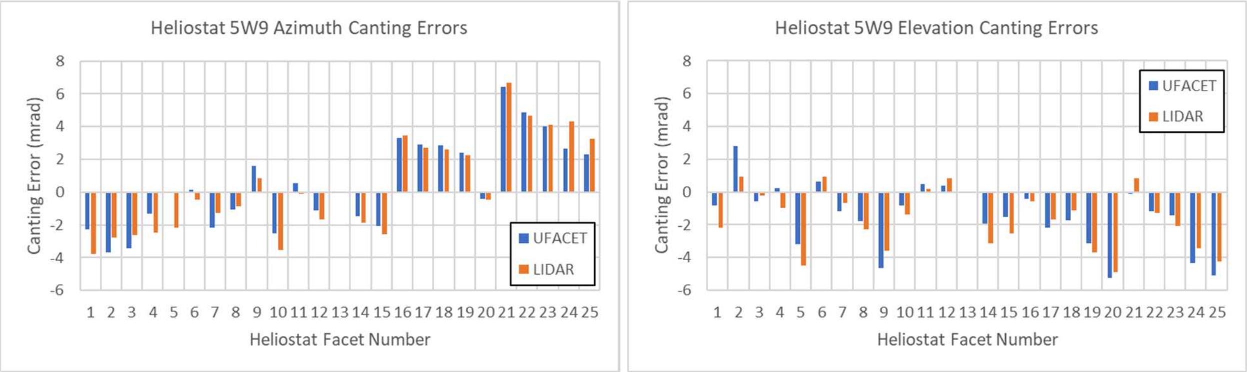

**FIGURE 9.** Heliostat 5W9 canting errors in azimuth (left) and elevation (right) directions as measured with UFACET method (blue) and a commercial LIDAR system (orange).

Figure 10 shows the canting error estimates on heliostat 9W1 from both the UFACET (blue) and LIDAR (orange) systems. In this case, three images (at varying camera distances) were analyzed with the UFACET processing code. The error bars represent 1σ variation between the three images. The RMS difference between UFACET and the LIDAR system was around 1.0 mrad in this case for both azimuth and elevation directions. There are two potential reasons for the higher RMS difference in this case. First, the UAS camera lens focal length was not sufficient to fill the heliostat in the field-of-view. This reduced the pixel density on the image of the heliostat under assessment. The effective low resolution of the images reduced the canting error calculation accuracy. Second, the LIDAR system relies on the soiling level on the mirror facets. A higher soiling level increases the accuracy, otherwise the mirrors become too specular for the LIDAR beam to return to the sensor head. For these measurements the facet soiling was low leaving some missing data on several facets. However, for initial measurements, the data trends for both UFACET and LIDAR are similar giving confidence the UFACET is measuring the facet canting correctly. In the future, imaging hardware and data collections will be improved.

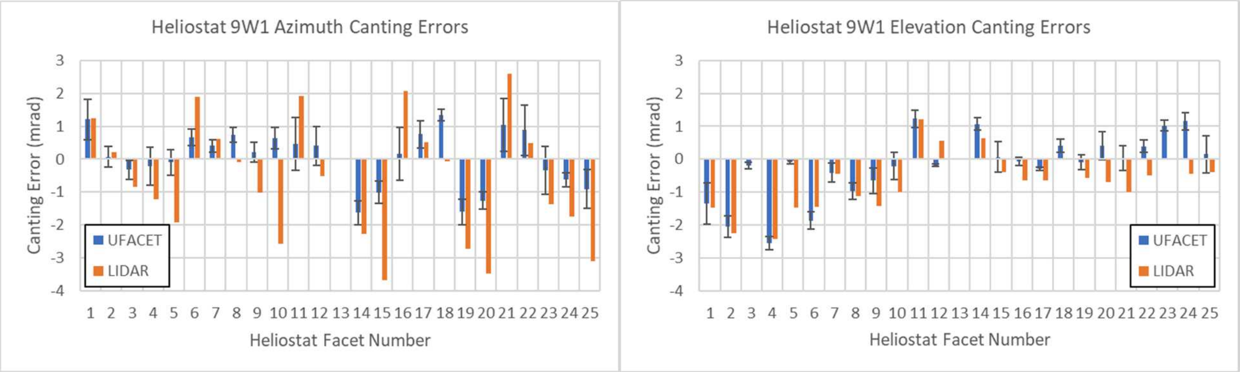

**FIGURE 10.** Heliostat 9W1 canting errors in azimuth (left) and elevation (right) as measured with UFACET method and a commercial LIDAR system.

## Initial Sensitivity Analysis

In this section, we provide our initial sensitivity analysis of the UFACET method. In this initial sensitivity analysis, we evaluated the impacts on the canting error calculations from position uncertainties on the assessed and target heliostats, target features, and UAS/camera. These are shown in Table 3 along with the uncertainty values associated with each parameter. Since the calculations are performed in a three-dimensional space, the uncertainties are defined over spherical bounds with diameters listed in Table 3. The uncertainty values are our initial estimates and are uniformly distributed. The impact on the canting error calculation is then determined from Monte Carlo simulations of 1,000+ scenarios. First, the impacts from the individual parameters were determined. Then the impact from all the parameters at once was simulated.

**TABLE 3.** Positional uncertainty values (at 1σ) used for sensitivity analysis.

| Parameter | Uncertainty (over 3D spherical diameter) |
|---|---|
| Assessed heliostat position | 2 cm |
| Target heliostat position | 2 cm |
| Target feature position | 1 cm |
| Camera position | 8 cm* |

* Assumes UAS with GPS + real-time kinematics (RTK) positioning.

Figure 11 shows the output of the Monte Carlo simulations using one of the 5W3 heliostat images. The results show the target heliostat position has the highest sensitivity. This becomes evident when considering that the target heliostat is viewed in reflection. Any movement of the facet causes larger apparent movements of the target heliostat from the camera's point of view. The camera position uncertainty appears to be less sensitive.

In general, the position uncertainty of each parameter causes around 0.5 mrad or less of canting error uncertainties. However, the position uncertainty values may be overestimated, particularly for the target feature positions. These features are constrained in the plane of the heliostat or other target structure, therefore assigning it a spherical uncertainty bound is an overestimation. Therefore, these results can be taken as worse case.

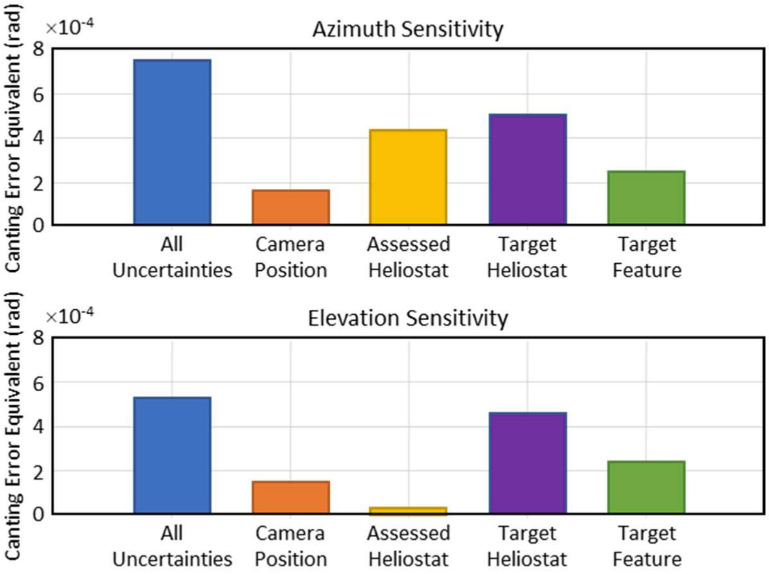

**FIGURE 11.** Results of the Monte Carlo sensitivity analysis using one of the 5W3 heliostat images.

## CONCLUSIONS

The optical performance of power tower heliostat collector fields can be impacted by slope errors, canting errors, tracking error, and soiling. The reduced optical performance can lead to negative impacts on the plant performance and financial revenues. A common issue is CSP operators do not have access to accurate or efficient field tools to measure the optical errors and subsequently fix the errors to improve the field optical performance. Existing tools are usually inefficient (i.e., time consuming, laborious, etc.), difficult to use or implement, and limited in accuracy. Sandia is developing an aerial imaging system to assess heliostats for canting errors while the heliostats are in-situ or offline. Performing in-situ measurements reduces interruptions to plant operations. Many heliostats can be measured within the flight time, usually 15-20 minutes, of the UAS. The collected images are then post-processed to calculate facet canting errors relative to an on-axis or off-axis canting strategy.

Initial results were presented for two heliostats (5W9 and 9W1). The results from the UFACET method were compared to measurements performed with a commercial LIDAR system. The RMS difference between the two methods were around 0.8 mrad in one case and 1.0 mrad for the other case. Some potential causes for reduced measurement accuracies were discussed. In the future these will be addressed with improved hardware and data collections. The initial sensitivity analysis showed the target heliostat position uncertainty had higher impact on the canting error calculations than the assessed heliostat and camera position uncertainties.

## FUTURE WORK

A few additions and improvements are under development and will be reported on in the future. These include improved imaging hardware, automated steps such as automatic heliostat edge and corner detections, incorporating machine learning to assist with the automated detections, and scanning of the reflected target across the heliostat under assessment to get estimates of the slope errors over the full facets. The more challenging portion is the automated detections of the reflected target features. This is where machine learning might also be applicable. A big milestone is then to demonstrate the system on a commercial collector field.

## ACKNOWLEDGEMENTS

Sandia National Laboratories is a multimission laboratory managed and operated by National Technology & Engineering Solutions of Sandia, LLC, a wholly owned subsidiary of Honeywell International Inc., for the U.S. Department of Energy's National Nuclear Security Administration under contract DE-NA0003525. The authors thank the project supporting team: Benson Tso, Jeremy Sment, Luis Garcia, Roger Buck, and Joshua Christian.

## REFERENCES

1. US Department of Energy, SunShot Vision Study, 2012.
2. J. Yellowhair, C.K. Ho, Heliostat Canting and Focusing Methods: An Overview and Comparison, ES2010-90356, *Proceedings of the ASME 2010 4th International Conference on Energy Sustainability.*
3. E. Sproul, K. Chavez, J. Yellowhair, Heliostat Focusing and Canting Enhancement Technique: An Optical Heliostat Alignment Tool for the National Solar Thermal Test Facility," ES2011-54268, *Proceedings of the ASME 2011 5th International Conference on Energy Sustainability*, Washington, D.C, Aug. 7-10.
4. K. Chavez, E. Sproul, J. Yellowhair, Heliostat Facet Focusing and Characterization using the Heliostat Focusing and Canting Enhancement Technique, *Proceedings of the ASME 2012 6th International Conference on Energy Sustainability*, San Diego, CA, July 23-26.
5. J. Yellowhair, *Field Guide to Solar Optics* (SPIE Press, Bellingham Washington, 2020), pp. 30-31.
6. C. Q. Little, D. E. Small, J. Yellowhair, LIDAR for Heliostat Optical Error Assessment, *Proceedings of SolarPACES 2020 Online Conference*, Sept. 28 – Oct. 2.
7. P. A. Apostolopoulos, J. Yellowhair, D. E. Small, D. Novick, M. Mann, UAS Imaging Path Planner for Heliostat Canting Assessments, *Proceedings of SolarPACES 2020 Online Conference*, Sept. 28 – Oct. 2.